

Contrastive Cross-Modal Pre-Training: A General Strategy for Small Sample Medical Imaging

Gongbo Liang, *Member, IEEE*, Connor Greenwell, *Student Member, IEEE*,
Yu Zhang, *Student Member, IEEE*, Xin Xing, *Student Member, IEEE*, Xiaoqin Wang,
Ramakanth Kavuluru, and Nathan Jacobs, *Senior Member, IEEE*

Abstract—A key challenge in training neural networks for a given medical imaging task is often the difficulty of obtaining a sufficient number of manually labeled examples. In contrast, textual imaging reports, which are often readily available in medical records, contain rich but unstructured interpretations written by experts as part of standard clinical practice. We propose using these textual reports as a form of weak supervision to improve the image interpretation performance of a neural network without requiring additional manually labeled examples. We use an image-text matching task to train a feature extractor and then fine-tune it in a transfer learning setting for a supervised task using a small labeled dataset. The end result is a neural network that automatically interprets imagery without requiring textual reports during inference. This approach can be applied to any task for which text-image pairs are readily available. We evaluate our method on three classification tasks and find consistent performance improvements, reducing the need for labeled data by 67%–98%.

Index Terms—Annotation-efficient modeling, pre-training, convolutional neural network, text-image matching

I. INTRODUCTION

Convolutional neural networks (CNNs) have been rapidly adopted in the medical domain [1]–[7]. However, robust CNNs are typically trained using large quantities of manually annotated data [8]–[11], such as ImageNet [12], which contains over one million images with discrete labels. Though large number of images are acquired each year in the medical domain, the number of images with manually annotated labels remains quite small due to the high annotation cost [13]–[15]. For instance, the cancer imaging archive (TCIA), one

of the largest collections of cancer images that is available for public download, hosted 127 datasets as of December 1st, 2020; only six of them contain more than 1000 cases, and a majority (80 out of 127) have fewer than a hundred cases [16]. The limited number of manually annotated images presents a barrier to adopting modern deep learning techniques in the medical imaging domain [13]–[15], [17].

In contrast to manually annotated labels, textual imaging reports, which are often readily available in medical records, contain interpretations written by experts as part of standard clinical practice (Figure 1). These unstructured textual data provide rich information about the images, but it is difficult to directly integrate the data into CNN training as labels.

We propose to use the textual imaging reports as a weak supervision signal. Our model gleans the associations between text and images through a text and image matching network that we call TIMNet (Text-Image Matching Network). The network learns the image features from a large number of text-image pairs. These training pairs include both positive examples of images and associated reports and those that randomly pair an image with a report not associated with it. In this sense, our loss function learns to contrast cross-modal pairs that are valid matches with those that do not correspond to the same diagnostic imaging event. Various models for a downstream application can then be built using the pre-trained image feature extractor. Intuitively speaking, TIMNet transfers the strong expert generated language signal to the image feature part of the architecture, priming it more powerfully for downstream training on supervised tasks. Since the feature extractor is pre-trained on a large and relevant dataset, transfer learning can be applied when building a downstream application that allows only a small labeled dataset to be used [18].

Our method is widely applicable in the medical imaging domain, in which textual reports are often readily available but obtaining manual labels is expensive. We demonstrate our method on three classification tasks, but our method uses textual data in a general way that is not limited to specific image analysis tasks. Our experimental results show that the proposed method reduces the need for manually annotated data by up to 98%. Our contributions in this work are as follows:

- we propose a novel weakly supervised method of pre-training medical imaging analysis networks, which learns

Submitted for review on December 23, 2020.

This work was sponsored by Grant No. IIS-1553116 from the U.S. National Science Foundation and Grant No. IRG-19-140-31 from the American Cancer Society.

Gongbo Liang was with the Department of Computer Science, University of Kentucky, Lexington, KY 40506 USA. Now, he is with the Department of Computer Science, Eastern Kentucky University, Richmond, KY 40475 USA. (e-mail: gongbo.liang@eku.edu).

Connor Greenwell, Yu Zhang, Xin Xing, and Nathan Jacobs are with the Department of Computer Science, University of Kentucky, Lexington, KY 40506 USA (e-mail: {connor.greenwell, y.zhang, xxi242, nathan.jacobs}@uky.edu).

Xiaoqin Wang is with the Department of Radiology, University of Kentucky, Lexington, KY 40536 USA (e-mail: xiaoqin.wang@uky.edu).

Ramakanth Kavuluru is with the Division of Biomedical Informatic, University of Kentucky, Lexington, KY 40536 USA (e-mail: ramakanth.kavuluru@uky.edu). His effort has been funded by the U.S. National Cancer Institute via grant P30CA177558.

The code is available at www.gb-liang.com/TIMNet



FINAL REPORT

HISTORY: ___-year-old female with chest pain.

COMPARISON: Comparison is made with chest radiographs from ___.

FINDINGS: The lungs are well expanded. A retrocardiac opacity is seen which is likely due to atelectasis although infection is hard to exclude. Given the linear shape of the opacity, atelectasis is perhaps more likely. The heart is top-normal in size. The cardiomeastinal silhouette is otherwise unremarkable. There is no pneumothorax or pleural effusion. Visualized osseous structures are unremarkable.

IMPRESSION: Retrocardiac opacity, likely due to atelectasis but possibly due to pneumonia in the appropriate setting.

Fig. 1: An example of a chest x-ray (left) with the radiology report (right) from the MIMIC-CXR dataset.

image features from a large but unlabeled dataset with associated textual reports;

- we demonstrate the proposed method via three classification tasks and also investigate the transferability of the learned features between datasets;
- we discuss the challenges of this study and provide a clear research direction for future researchers.

II. BACKGROUND

A. Textual Data in Image Analysis

Researchers are actively seeking solutions for using textual data effectively in the field of medical imaging analysis. However, most works focus on deriving manual labels from textual data in different ways. For instance, CheXpert [19] and NegBio [20] propose two natural language processing (NLP) algorithms that are used for clinical text parsing. Both of these algorithms can extract keywords (e.g., pneumonia and pulmonary edema) from text that can be used as image-level labels. They can also assign attributes to the extraction keywords, such as positive pneumonia or negative pulmonary edema. Although such kinds of NLP tools are useful in automatically labeling a large amount of data, the accuracy of the derived labels can be an issue. As shown in [21], the automatically generated labels do not always agree with each other in a large number of cases.

In addition to deriving discrete labels purely from clinical textual data, researchers also combine text and images for inferring labels during network training [22]–[25]. For instance, Wu et al. proposed a weakly supervised method for chest X-ray abnormality localization [22]. This method first predefined six pseudo-bounding boxes for different lung zones in each of the input images. Then, the normal and abnormal labels of the pseudo-bounding boxes can be derived from the associated text imaging report. Finally, the labeled pseudo-bounding boxes are used to train a localization network. Such a method can train medical imaging analysis networks end-to-end using textual data as supervision. However, label deriving with NLP tools is still need during the training. The network performance may heavily rely on the accuracy of the derived labels.

Instead of deriving labels from the clinical textual data, we propose using the textual data as weak supervision for

image feature learning through text-image matching tasks. Our method uses textual data in a general way that is not limited to specific image analysis tasks. More importantly, there is no need to train a separate NLP model that is independent of the image analysis tasks for inferring labels.

B. Text and Image Matching

Text-image matching has become a popular research topic in recent years. Broadly, the existing matching methods can be divided into two categories: 1) local representation matching and 2) global representation matching.

Local representation matching focuses on local feature matching between text and images. For instance, we can extract objects from images and then match the objects to words in a given text [26]–[30]. One drawback of the local representation matching method is that it usually relies on pre-trained object detectors, such as R-CNNs [31]–[33]. However, a pretrained, high-performance object detector is usually not available in the medical imaging domain.

The global representation matching method usually involves three procedures: 1) image feature embedding, 2) text feature embedding, and 3) measures of the distance between the two embeddings. For instance, Kiros et al. [34] used a CNN to encode images and a long short-term memory network (LSTM) [35] to encode the full text. The triplet loss is used to pull the embeddings of the matched text and image closer to each other and push the unmatched ones further apart. Wehrmann et al. [36] encoded the text data using an efficient character-level inception module that convolves over characters in the text. Sarafianos et al. [37] trained a text-image matching network by using a ResNet101 [8] network for imaging processing and a transformer-based model [38] with an LSTM based encoder for text processing.

Most of the prior efforts focused on the matching problem from the perspective of text-based querying systems for image retrieval. In contrast, we aim to imbue image analysis models with the knowledge obtained from learning to match a medical image with the associated clinician-generated textual report.

C. Natural Language Encoding

Natural language encoding represents words as dense embeddings in a real vector space instead of the typical multi-hot encoding. Word2vec [39], [40] is a famous approach that hypothesizes that similar words tend to share distributional similarities, appearing in similar contexts or the same contexts. However, the drawback of this method is that the embedding is independent of the context in which the word appears. Thus, this method cannot address polysemy or homonymy.. Contextualized embeddings use a language modeling-based objective for self-supervision that predicts words based on prefixes in longer snippets of text, which overcomes the limitation of word2vec in addressing polysemy and homonymy issues.

The transformer [41] architecture uses an encoder-decoder structure and attention mechanism to translate one sequence to another sequence. It can encode the contextual information of a word from distant parts of a sentence. Unlike a conventional recurrent neural network (RNN), a transformer does not require sequential data to be processed in order, leading to new practical gains in efficiency. The *bidirectional encoder representations from transformers* (BERT) [38] architecture trains a transformer by jointly conditioning on both left and right contexts in all layers. A pre-trained BERT model can be fine-tuned to create state-of-the-art models for various tasks without substantial task-specific architectural modifications [42], [43]. In this study, we use a pre-trained BERT model as the text processing branch that encodes a given text as a feature vector.

III. METHOD

We assume two datasets (X_P and X_L) exist, where X_P has paired 2-tuples of images and associated textual reports and X_L consists of labeled images. Specifically, $X_P = \{(x_i^{(j)}, x_t^{(j)}) : x_i^{(j)} \in x_i, x_t^{(j)} \in x_t\}$ is an image and text paired dataset where x_i is a set of images and x_t is a set of textual notes such that $x_t^{(j)}$, the j -report, corresponds to $x_i^{(j)}$, the j -th image. Also, $X_L = \{x_l, y\}$ is a labeled imaging dataset, where x_l is a set of images and y represents the set of corresponding labels, which could be image-level labels, bounding boxes, or pixel-level labels. Typically, we have $|X_L| \ll |X_P|$.

We first learn an image encoding function f using X_P that encodes x_i to a feature space. Then, f can be used to build a downstream application using X_L that maps x_l to y . We learn f through TIMNet, which predicts whether a given pair of (x_i, x_t) is naturally related.

The proposed idea is illustrated in Figure 2. The network consists of two modules: 1) a weakly supervised image feature learning module and 2) a downstream application module for a specific task. The image encoding function f is a CNN image feature extractor that is shared between the modules.

A. Weakly Supervised Image Feature Learning

Weakly supervised image feature learning, i.e., image encoding is carried out through a global cross-modal matching approach with a two-branch network, one for text processing

and the other for imaging processing. The input of the network is a text-image pair with a label indicating whether the text and image correspond to the same imaging event. The pair of the text and image is first projected into a vector space. Then, the absolute difference between the two output feature vectors is fed to a classification network, which predicts whether the input image and text are a true pair.

Mathematically, the text processing branch is defined as:

$$v_t^{(j)} = h_t(x_t^{(j)}), \quad (1)$$

where $h_t(\cdot)$ is the text processing network, $x_t^{(j)}$ is the j^{th} input text, and $v_t^{(j)}$ is the output vector. The network is composed of a BERT encoder, a 1×1 convolutional (Conv) layer, a global average pooling (GAP) layer, and a fully-connected (FC) layer. The BERT encoder is used as a text feature extractor, which encodes the input text as contextualized embedding vectors. The vectors are then passed through the 1×1 Conv layer following GAP. The FC layer projects the vectors into a feature space as a feature vector. The image processing branch is defined as:

$$v_i^{(j)} = h_i(x_i^{(j)}), \quad (2)$$

where $h_i(\cdot)$ is the image processing network, $x_i^{(j)}$ is the j^{th} input image, and $v_i^{(j)}$ is the output feature vector. The Conv layers of a ResNet model [8] are used as a feature extractor in $h_i(\cdot)$. An FC layer is added after the feature extractor that projects the image features into a feature space as a feature vector. The absolute difference of $v_t^{(j)}$ and $v_i^{(j)}$ is then passed to a shallow classification network, $h_{cls}(\cdot)$, for the matching prediction. Cross-entropy loss is used during the training of $h_{cls}(\cdot)$ to contrast valid matches from mismatched instances.

In general, the global matching network for weakly supervised image feature learning is expressed as:

$$h(x^{(j)}) = h_{cls}(|h_t(x_t^{(j)}) - h_i(x_i^{(j)})|), \quad (3)$$

where $x^{(j)}$ is the j^{th} input, $x^{(j)} = \{x_t^{(j)}, x_i^{(j)}\}$, $x^{(j)} \in X_P$, $|\cdot|$ denotes the absolute difference, and $h(\cdot)$ is the whole matching network. The absolute difference combining with cross-entropy loss forms a contrastive-style network that learns image features under a weakly supervised fashion.

B. Fine-Tuning for Downstream Tasks

At the end of the weakly supervised feature learning phase described earlier, the hypothesis is that the matching process has pre-trained the parameterized image feature extractor f to the extent that it needs fewer supervised instances for a downstream image-related task. This, in turn, relies on our high-level intuition that there is a nontrivial transferable signal available in the textual annotations to improve imaging tasks down the line.

The fine-tuning of the image processing branch in TIMNet for downstream tasks is fairly straightforward. Although it can be done for a variety of applications, in this study, we demonstrate the proposed method for classification tasks.

To build a downstream application model, we can either add additional Conv layers and FC layers to the image processing branch $h_i(\cdot)$, or use it as-is by retraining the FC layers. Since

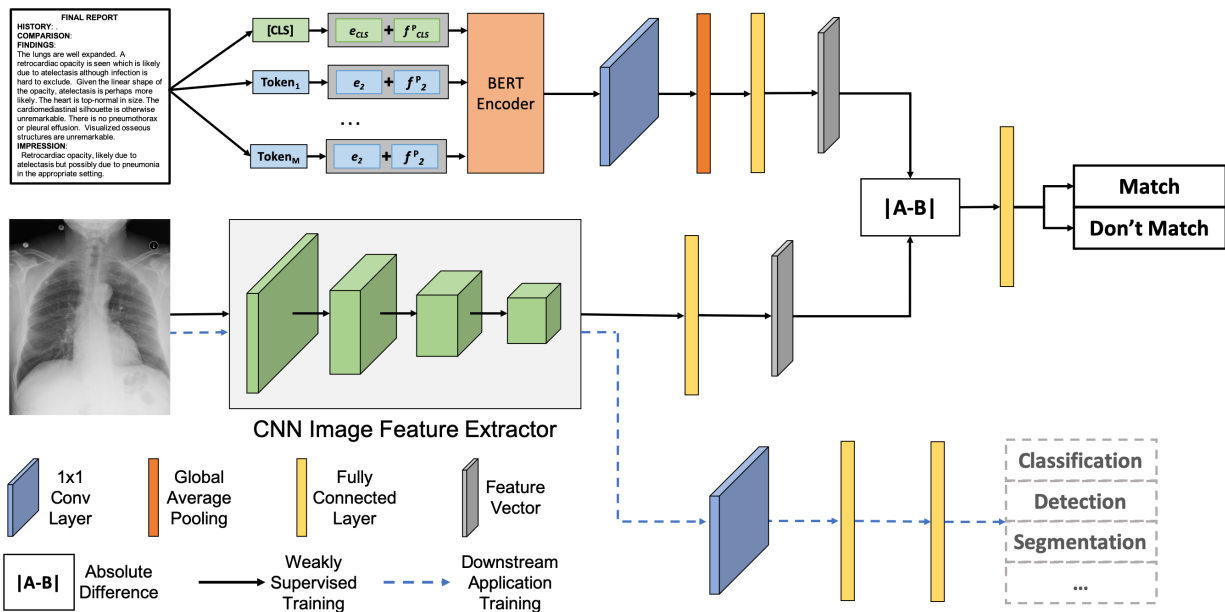


Fig. 2: The TIMNet cross-modal matching architecture. 1) weakly supervised image feature learning through a text-image matching network (solid black line). 2) Downstream application training using a small dataset (dashed blue line).

we need to optimize only the few additional layers from scratch, while the rest of the network is already pre-trained on a larger set of images from the same domain, the total number of required training instances for fine-tuning can be much smaller than training the entire network from scratch.

C. Implementation

The HuggingFace BERT with `bert-base-uncased` weights [44] is used as the backbone of the text processing branch. A 1×1 Conv layer, a GAP layer, and an FC layer with 512 neurons are added to the BERT encoder. The ResNet-18 model is used as the backbone of the imaging processing branch. A 1×1 Conv layer and an FC layer with 512 neurons are added before and after the GAP layer, respectively. Both of the 1×1 Conv layers in the text processing and image processing branches are followed by batch normalization [45] and a rectified linear unit (ReLU) [46].

All the Conv layers of the image processing branch are used as a feature extractor in the downstream networks. A shallow CNN classification network is added on top of the feature extractor. The CNN classification network contains a 1×1 Conv layer, an FC layer with 512 neurons, and an output layer with various numbers of neurons for different tasks. Cross-entropy loss and an Adam optimizer [47] with a learning rate of 0.0001 are used for both the weakly supervised feature learning stage and the downstream application training stage.

IV. EVALUATION AND DISCUSSION

A. Datasets

We use the MIMIC-CXR [21] and Mendeley-V2 [48] datasets in this study. The MIMIC-CXR dataset is used in both the TIMNet pre-training and downstream application training. Mendeley-V2 is used only for downstream application training.

1) *MIMIC-CXR*: This dataset contains 227,835 radiographic studies of 64,588 patients with 368,948 chest X-rays and the associated radiology reports. The dataset also provides 14 labels (with 13 labels for different abnormalities and one label for the normal case), which are derived from the radiology reports using NLP tools [19], [20]. In the official training/validation/testing split, the validation set and test set have 2,991 and 5,159 images, respectively. We combine the official validation and test sets to form our validation set. The chest X-ray images are resized to 500×500 . We use the official training set and our validation set in both TIMNet pre-training and downstream application training.

2) *Mendeley-V2*: This dataset is a pediatric chest X-ray dataset that includes 4,273 pneumonia images and 1,583 normal images. Although the imaging modality is the same as that of MIMIC-CXR, the patient demographics are different. In addition, the images in Mendeley-V2 may have been acquired with devices from different vendors. We used the original training/validation split of this dataset to train a downstream application model that evaluates the transferability of pre-trained weights between different datasets while retaining the same imaging modality.

B. Evaluation Setup

We evaluate the proposed method through the downstream application performance and the degree of need for labeled instances for supervision. We denote the downstream models with the TIMNet pre-trained weights as *Ours* and models without the pre-trained weights as *Base*.

1) *Weakly Supervised Feature Learning*: The feature extractor in *Ours* is pre-trained for 50 epochs using the text-image pairs from the training set of MIMIC-CXR. During the training, we ensure that the numbers of true pairs and false

pairs are balanced. The “findings” portion of the radiology reports is used as the text input. The length of each piece of text is preprocessed to 256 words at the word embedding stage. We add 0s for texts shorter than 256 words, and we snip much longer texts to 256 words. The output of this first weak-supervision phase is a probability estimate of the input text-image pair being a true match.

2) *Downstream Applications:* The downstream networks for both *Ours* and *Base* are trained using varying amounts of the training data and image-level labels from the MIMIC-CXR and Mendeley-V2 datasets, ranging from 0.5% to 100%. Three downstream applications are trained, namely, 1) a binary classification model for abnormality diagnosis of MIMIC-CXR; 2) a multi-label classification model for lung disease diagnosis of MIMIC-CXR; and 3) a binary classification model for pediatric pneumonia diagnosis of Mendeley-V2. Each downstream network is trained for 100 epochs with a batch size of 16 for three trials. No text is needed for training the downstream networks. We use the accuracy (ACC), the area under the receiver operating characteristic curve (auROC), precision (Prec), recall (Recall), F1 score (F1), and average precision (AP) as the evaluation metrics for the binary classification tasks and the auROC and AP for the multi-label classification tasks. The results reported in this paper are the average performances over all trials.

C. Classification on MIMIC-CXR

We first present the evaluation results of downstream applications that are trained using the MIMIC-CXR dataset. Two downstream application models are trained and tested: a binary classification model and a multi-label classification model. The binary classification model predicts whether an abnormality exists in an image, and the multi-label classification model predicts what kind of abnormality exists in an image. The output of the binary classification model is Boolean, and the output for the multi-label task is a multi-hot vector, with 1 indicating the presence of a particular class.

1) *Binary Classification:* Figure 3 shows the result of the binary classification task on the MIMIC-CXR dataset. The results reveal that the proposed method has superior performance to that of the *Base* model in all settings, with better gains when only a few labeled images are available. For instance, when using 0.5% of labeled data ($\approx 1,800$ instances), the *Base* model has an accuracy of 66.41%, while the *Ours* has a 71.81% accuracy. The highest accuracy of *Base* is 76.38%, when it is trained with 90% of the labeled data ($\approx 325,000$ instances). *Ours* surpasses the best performance (across all metrics) of *Base* with only 30% of the training data ($\approx 108,000$ instances). Thus the need for manual labels is reduced by 67% when using the proposed method. See Table S1 (supplementary data, after the references) for more detailed results. One particular observation is that for every fraction of the full training dataset considered, TIMNet is superior across all measures except recall. There is no clear winner for recall, but TIMNet still scores better across most settings (7 out of 11 training fractions).

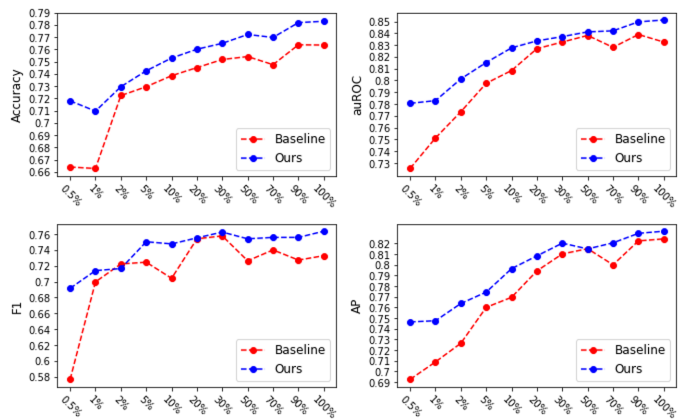


Fig. 3: Binary classification results on MIMIC-CXR dataset.

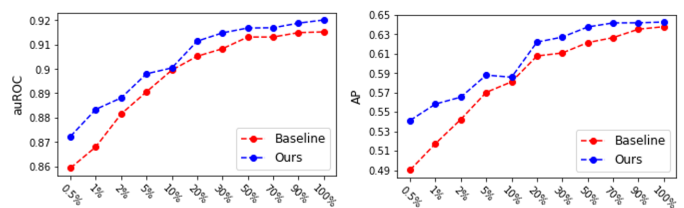


Fig. 4: Multi-label learning results on MIMIC-CXR dataset.

2) *Multi-Label Classification:* Figure 4, the multi-label classification results on MIMIC-CXR, also shows the superior performance of *Ours* compared to the *Base* model. As in the binary case, TIMNet is able to significantly reduce the need for manual labels while achieving a comparable performance. The *Base* model reaches its best performance (0.9152 auROC) with 100% of the training data, while *Ours* can achieve a similar performance (0.9148 auROC) with only 30% of the training data. Additional details of the specific scores are presented in Table S2.

D. Transferability of the Pre-Trained Weights

The feature extractor used in *Ours* is pre-trained via TIMNet on MIMIC-CXR, a chest X-ray dataset. In this section, we evaluate the transferability of these pre-trained weights between different datasets. More specifically, we assess the downstream model performance on Mendeley-V2, which is a pediatric chest X-ray dataset for pneumonia. The imaging modalities of MIMIC-CXR and Mendeley-V2 are the same, but the patient demographics are different.

Figure 5 shows the model performance for pneumonia diagnosis on the Mendeley-V2. The results show that TIMNet’s pre-trained features work surprisingly well, and it is able to reduce the need for labeled data by 98.33%, as elaborated next. The *Base* model achieves its highest accuracy of 87.52% using 30% of the training data, and the highest auROC of 0.9333 also uses 30% of the training data, while *Ours* outperforms *Base* with using only 0.5% of training data with an 88.14% accuracy and a 0.9352 auROC. Thus the reduction in training instances is $(30 - 0.5)/30 = 98.33\%$. The highest performances of *Ours* are 91.87% accuracy and 0.9613 auROC. These are also nearly

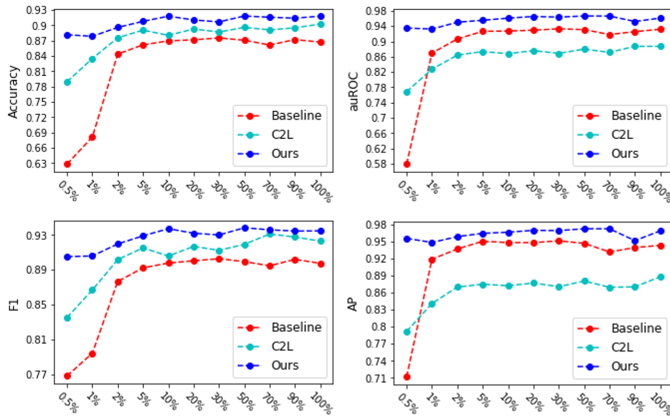


Fig. 5: Binary classification results on Mendeley-V2 dataset.

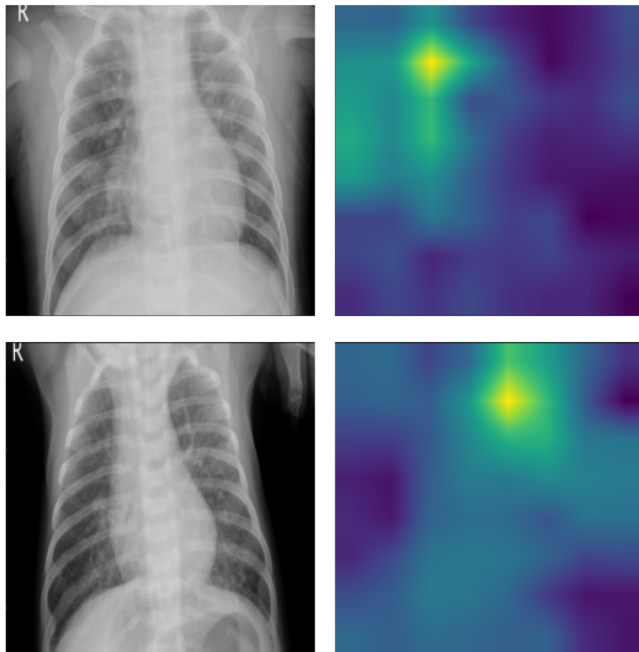


Fig. 6: Two CAM visualizations for pediatric chest X-ray pneumonia classification on the Mendeley-V2 dataset with chest X-ray on the left and CAM on the right. The CAMs reveal that the model correctly focuses on the corresponding areas that show some concerns about pneumonia.

5% (ACC) and 3% (auROC) higher than those of the *Base* model. Please see Table S3 for more details.

Figure 6 shows two class activation mapping (CAM) [49] visualizations for the pediatric pneumonia diagnosis model. The pixel values in the CAMs are associated with the contribution to the classification decision. A higher value (brighter color) indicates a higher contribution to the class decision. Both cases in the figure are ground-truth positive cases. The CAMs reveal that the model correctly focuses on the corresponding areas that show some concerns about pneumonia.

E. Discussion

We propose learning meaningful feature representations of medical images using TIMNet via a text-image matching task

TABLE I: Text and image matching results

Dataset	Accuracy	auROC	F1 Score	Prec	Recall	AP
MIMIC-CXR	0.74	0.83	0.74	0.67	0.82	0.77

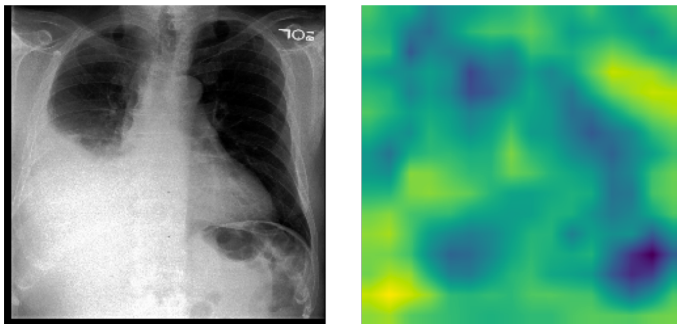
without acquiring additional manually labeled annotations. Our method can help build effective models for downstream predictions that rely only on image input. During our experiments, we discovered that better text-image matching performances usually lead to improved downstream application performances in terms of higher accuracy and reduced need for labeled images. The pre-trained TIMNet used in this study has a text-image matching performance of 74% accuracy and 0.83 auROC. Table I shows the relevant results of the evaluation.

Figure 7 shows CAM visualizations of TIMNet on the text-image matching task. The findings of the radiology reports are displayed below the images. The CAMs suggest that the decisions made by TIMNet are reasonable. For instance, in Figure 7a, the radiology report indicates increased right-sided pleural effusion, and CAM shows more significant contributions near the effusion areas on the right-hand side of the figure. Figure 7b shows a similar correspondence between the CAM-based image segment contributions to the model decision and the textual report.

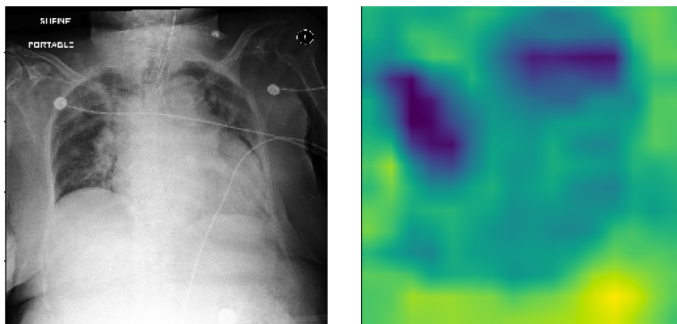
Notably, text-image matching tasks in the medical domain are often more challenging than in the natural imaging domain, for several reasons. First, textual data in the natural imaging domain usually contain much fewer words. For instance, the vast majority of image captions in the natural imaging domain contain 7 to 15 words [50]. However, this number can easily reach 10x higher or more in the medical imaging domain [21]. Second, the uncertainty of the language in the medical imaging domain is often higher. For example, the findings of Figure 7b are, “moderate cardiomegaly and appears to have progressed since prior *could potentially* being part due to changes in positioning.” Such uncertain statements are usually not found in natural imaging captions. Third, the textual reports in the medical imaging domain often contain information that cannot be seen in the image, such as the findings of Figure 7a, which mention that “the cardiac, mediastinal and hilar *contours appear unchanged*.” Without comparison with previous studies, the network may not be able to link the words “*contours appear unchanged*” to any regions in the image. Fourth, multiple abnormal conditions might co-exist with multiple normal conditions for the same patient. All these challenges make text-image matching a difficult task in the medical imaging domain.

V. CONCLUDING REMARKS

The main objective of our work is to demonstrate the potential of the clinician-authored textual reports that accompany most medical images in improving image-related supervised ML applications by pretraining a feature extractor without requiring additional manually labeled annotations. Such textual narratives are readily available and routinely curated as part of healthcare operations and are therefore a natural resource to leverage. The central premise of our effort is the insight that in a latent neural dense vector representation space, it



(a) FINDINGS: The cardiac, mediastinal and hilar contours appear unchanged. There is no shift of mediastinal structures. There is a large right-sided pleural effusion, which has increased since the earlier radiographs and perhaps slightly since the more recent CT. There is no pneumothorax. The left lung remains clear.



(b) FINDINGS: ET tube is seen with tip approximately 1.8 cm from the carina. Enteric tube seen passing below the inferior field of view. Lower lung volumes are noted on the current exam with bilateral parenchymal opacities which could be due to edema or infection. Prominence of the right hilum is again noted. Moderate cardiomegaly and appears to have progressed since prior could potentially being part due to changes in positioning. No acute osseous abnormalities. Surgical clips project over the left chest wall/axilla.

Fig. 7: CAM visualizations of text and image matching on MIMIC-CXR with chest X-ray on the left and CAM on the right. The CAMs reveal that the model focuses on the corresponding areas that show some concerns in the textual findings.

may be possible to transfer linguistic signals that characterize expert summaries of images to downstream image-based tasks through weak supervision. Based on the experiments and evaluations in this paper, we believe we have successfully verified this insight for classification tasks.

At the core of our methodology is a two-branch architecture, TIMNet, that identifies whether a textual finding corresponds to the supplied image. The main purpose of text-image matching tasks is to use the textual finding as weak supervision to learn the image feature representations. In this way, the feature extractor is trained on a large and relevant dataset without requiring additional manually labeled annotations. Subsequently, the image branch is further fine-tuned for downstream supervised tasks using a small labeled dataset. Our experiments show that with the proposed method, small fractions (2%–30%) of the available full training data are needed to achieve the same performance as baseline models that do not exploit textual reports. Additionally, the benefits

persist across datasets, which is an excellent benefit when transferring signals from models learned on deidentified textual reports (e.g., MIMIC-CXR) to other classification settings that have fewer or no textual annotations (due to HIPAA and other privacy restrictions).

During our experiments, we discovered that better text-image matching performances usually lead to improved downstream application performances. Thus, one of our future directions will be to further innovate the matching framework to improve the associated performance. Another important future direction is to see whether our text-image matching setup can actually transfer the image signal to downstream tasks in the NLP domain for clinical text. We believe this bidirectional feedback may help in extracting named entities (e.g., drugs, comorbidities, and anatomical sites) and relations connecting such entities (e.g., adverse drug reactions) from a variety of notes. These information extraction tasks are also usually plagued by a lack of large training datasets (esp. public ones) due to strict regulatory constraints governing textual data in medicine. Overall, we hope our work spurs further interest in exploring the synergy between text and images.

REFERENCES

- [1] V. Gulshan *et al.*, “Development and validation of a deep learning algorithm for detection of diabetic retinopathy in retinal fundus photographs,” *Jama*, vol. 316, no. 22, pp. 2402–2410, 2016.
- [2] A. Esteva *et al.*, “Dermatologist-level classification of skin cancer with deep neural networks,” *Nature*, vol. 542, no. 7639, pp. 115–118, 2017.
- [3] L. Liu, S. Yang, L. Meng, M. Li, and J. Wang, “Multi-scale deep convolutional neural network for stroke lesions segmentation on ct images,” in *International MICCAI Brainlesion Workshop*, 2018.
- [4] G. Liang, S. Fouladvand, J. Zhang, M. A. Brooks, N. Jacobs, and J. Chen, “Ganai: Standardizing ct images using generative adversarial network with alternative improvement,” in *Proc. IEEE Int. Conf. on Healthcare Informatics*, 2019.
- [5] R. P. Mihail, G. Liang, and N. Jacobs, “Automatic hand skeletal shape estimation from radiographs,” *IEEE Tran. on Nanobioscience*, vol. 18, no. 3, pp. 296–305, 2019.
- [6] Y. Zhang *et al.*, “2d convolutional neural networks for 3d digital breast tomosynthesis classification,” in *Proc. Int. Conf. on Bioinf. and Biomed. IEEE*, 2019.
- [7] X. Xing *et al.*, “Dynamic image for 3d mri image alzheimer’s disease classification,” in *Proc. Eur. Conf. Comput. Vis. Workshops*, 2020.
- [8] K. He, X. Zhang, S. Ren, and J. Sun, “Deep residual learning for image recognition,” in *Proc. IEEE Conf. Comput. Vis. Pattern Recogn.*, 2016.
- [9] G. Huang, Z. Liu, L. Van Der Maaten, and K. Q. Weinberger, “Densely connected convolutional networks,” in *Proc. IEEE Conf. Comput. Vis. Pattern Recogn.*, 2017.
- [10] A. Y. Hannun *et al.*, “Cardiologist-level arrhythmia detection and classification in ambulatory electrocardiograms using a deep neural network,” *Nature Medicine*, vol. 25, no. 1, pp. 65–69, 2019.
- [11] T. Falk *et al.*, “U-net: deep learning for cell counting, detection, and morphometry,” *Nature Methods*, vol. 16, no. 1, pp. 67–70, 2019.
- [12] J. Deng, W. Dong, R. Socher, L.-J. Li, K. Li, and L. Fei-Fei, “Imagenet: A large-scale hierarchical image database,” in *2009 IEEE conference on computer vision and pattern recognition*. Ieee, 2009, pp. 248–255.
- [13] G. Litjens *et al.*, “A survey on deep learning in medical image analysis,” *Med. Image Anal.*, vol. 42, pp. 60–88, 2017.
- [14] Y. Yu, M. Li, L. Liu, Y. Li, and J. Wang, “Clinical big data and deep learning: Applications, challenges, and future outlooks,” *Big Data Mining and Analytics*, vol. 2, no. 4, pp. 288–305, 2019.
- [15] M. J. Willemink *et al.*, “Preparing medical imaging data for machine learning,” *Radiology*, vol. 295, no. 1, pp. 4–15, 2020.
- [16] “The cancer imaging archive,” *The Cancer Imaging Archive (TCIA)*, 2020. [Online]. Available: <https://www.cancerimagingarchive.net/>
- [17] X. Wang, G. Liang, Y. Zhang, H. Blanton, Z. Bessinger, and N. Jacobs, “Inconsistent performance of deep learning models on mammogram classification,” *Journal of the American College of Radiology*, vol. 17, no. 6, pp. 796–803, 2020.

- [18] K. Mendel, H. Li, D. Sheth, and M. Giger, "Transfer learning from convolutional neural networks for computer-aided diagnosis: a comparison of digital breast tomosynthesis and full-field digital mammography," *Academic radiology*, vol. 26, no. 6, pp. 735–743, 2019.
- [19] J. Irvin *et al.*, "Chexpert: A large chest radiograph dataset with uncertainty labels and expert comparison," in *Proc. AAAI Conf. on Artif. Intel.*, 2019.
- [20] Y. Peng, X. Wang, L. Lu, M. Bagheri, R. Summers, and Z. Lu, "Negbio: a high-performance tool for negation and uncertainty detection in radiology reports," in *Proc. AMIA Summits on Trans. Sci.*, 2018.
- [21] A. E. Johnson *et al.*, "Mimic-cxr: A large publicly available database of labeled chest radiographs," *arXiv:1901.07042*, 2019.
- [22] J. Wu *et al.*, "Automatic bounding box annotation of chest x-ray data for localization of abnormalities," in *IEEE Int. Sympos. on Biomed. Imaging*, 2020.
- [23] L. K. Tam, X. Wang, E. Turkbey, K. Lu, Y. Wen, and D. Xu, "Weakly supervised one-stage vision and language disease detection using large scale pneumonia and pneumothorax studies," in *Proc. Int. Conf. on Med. Image Comput. and Comput.-Assist. Interv.* Springer, 2020.
- [24] M. Moradi, A. Madani, Y. Gur, Y. Guo, and T. Syeda-Mahmood, "Bimodal network architectures for automatic generation of image annotation from text," in *Proc. Int. Conf. on Med. Image Comput. and Comput.-Assist. Interv.*, 2018.
- [25] J. Yuan, H. Liao, R. Luo, and J. Luo, "Automatic radiology report generation based on multi-view image fusion and medical concept enrichment," in *Proc. Int. Conf. on Med. Image Comput. and Comput.-Assist. Interv.* Springer, 2019.
- [26] A. Karpathy, A. Joulin, and F.-F. Li, "Deep fragment embeddings for bidirectional image sentence mapping," in *Proc. Adv. Neural Inf. Process. Syst.*, 2014.
- [27] K.-H. Lee, X. Chen, G. Hua, H. Hu, and X. He, "Stacked cross attention for image-text matching," in *Proc. Eur. Conf. Comput. Vis.*, 2018.
- [28] L. Wang, Y. Li, J. Huang, and S. Lazebnik, "Learning two-branch neural networks for image-text matching tasks," *IEEE Trans. Pattern Anal. Mach. Intell.*, vol. 41, no. 2, pp. 394–407, 2018.
- [29] C. Liu, Z. Mao, T. Zhang, H. Xie, B. Wang, and Y. Zhang, "Graph structured network for image-text matching," in *Proc. IEEE/CVF Conf. Comput. Vis. Pattern Recogn.*, 2020.
- [30] S. Wang, R. Wang, Z. Yao, S. Shan, and X. Chen, "Cross-modal scene graph matching for relationship-aware image-text retrieval," in *Proc. IEEE Wint. Conf. on Appl. of Comput. Vis.*, 2020.
- [31] R. Girshick, J. Donahue, T. Darrell, and J. Malik, "Rich feature hierarchies for accurate object detection and semantic segmentation," in *Proc. IEEE Conf. Comput. Vis. Pattern Recogn.*, 2014, pp. 580–587.
- [32] R. Girshick, "Fast r-cnn," in *Proc. IEEE Conf. Comput. Vis. Pattern Recogn.*, 2015.
- [33] S. Ren, K. He, R. Girshick, and J. Sun, "Faster r-cnn: Towards real-time object detection with region proposal networks," in *Proc. Adv. Neural Inf. Process. Syst.*, 2015.
- [34] R. Kiros, R. Salakhutdinov, and R. S. Zemel, "Unifying visual-semantic embeddings with multimodal neural language models," *arXiv:1411.2539*, 2014.
- [35] S. Hochreiter and J. Schmidhuber, "Long short-term memory," *Neural Computation*, vol. 9, no. 8, pp. 1735–1780, 1997.
- [36] J. Wehrmann and R. C. Barros, "Bidirectional retrieval made simple," in *Proc. IEEE Conf. Comput. Vis. Pattern Recogn.*, 2018.
- [37] N. Sarafianos, X. Xu, and I. A. Kakadiaris, "Adversarial representation learning for text-to-image matching," in *Proc. IEEE Conf. Comput. Vis. Pattern Recogn.*, 2019.
- [38] J. Devlin, M.-W. Chang, K. Lee, and K. Toutanova, "BERT: Pre-training of deep bidirectional transformers for language understanding," in *Proc. of the 2019 Conf. of the North American Chapter of the Assoc. for Comput. Linguistics: Human Lang. Tech.*, 2019.
- [39] T. Mikolov, I. Sutskever, K. Chen, G. S. Corrado, and J. Dean, "Distributed representations of words and phrases and their compositionality," in *Proc. Adv. Neural Inf. Process. Syst.*, 2013.
- [40] T. Mikolov, K. Chen, G. Corrado, and J. Dean, "Efficient estimation of word representations in vector space," in *Proc. 1st Int. Conf. on Learn. Represent.*, 2013.
- [41] A. Vaswani *et al.*, "Attention is all you need," in *Proc. Adv. Neural Inf. Process. Syst.*, 2017.
- [42] C. Sun, X. Qiu, Y. Xu, and X. Huang, "How to fine-tune bert for text classification?" in *China National Conf. on Chinese Comput. Linguistics*. Springer, 2019.
- [43] J. Lee *et al.*, "Biobert: a pre-trained biomedical language representation model for biomedical text mining," *Bioinformatics*, vol. 36, no. 4, pp. 1234–1240, 2020.
- [44] T. Wolf *et al.*, "Huggingface's transformers: State-of-the-art natural language processing," *arXiv:1910.03771*, 2019.
- [45] S. Ioffe and C. Szegedy, "Batch normalization: Accelerating deep network training by reducing internal covariate shift," *arXiv preprint arXiv:1502.03167*, 2015.
- [46] V. Nair and G. E. Hinton, "Rectified linear units improve restricted boltzmann machines," in *ICML*, 2010.
- [47] D. P. Kingma and J. Ba, "Adam: A method for stochastic optimization," in *Proc. 3rd Int. Conf. on Learn. Represent.*, 2015.
- [48] D. Kermany and M. Goldbaum, "Labeled optical coherence tomography (oct) and chest x-ray images for classification," *Mendeley Data*, vol. 2, 2018.
- [49] B. Zhou, A. Khosla, A. Lapedriza, A. Oliva, and A. Torralba, "Learning deep features for discriminative localization," in *Proc. IEEE Conf. Comput. Vis. Pattern Recogn.*, 2016.
- [50] X. Hu *et al.*, "Vivo: Surpassing human performance in novel object captioning with visual vocabulary pre-training," *Proc. Eur. Conf. Comput. Vis.*, 2020.

Supplementary Materials

TABLE S1: Binary classification evaluation results on the MIMIC-CXR dataset

Metric	Model	Percentage of Training Data										
		0.5%	1%	2%	5%	10%	15%	30%	50%	70%	90%	100%
ACC	Base	0.6641	0.6629	0.7224	0.7296	0.7386	0.7452	0.7518	0.7542	0.7476	0.7638	0.7636
	Ours	0.7181	0.7097	0.7296	0.7426	0.7530	0.7602	0.7650	0.7722	0.7698	0.7819	0.7830
auROC	Base	0.7255	0.7513	0.7735	0.7976	0.8084	0.8269	0.8325	0.8381	0.8280	0.8389	0.8325
	Ours	0.7806	0.7829	0.8013	0.8152	0.8276	0.8335	0.8371	0.8411	0.8420	0.8496	0.8512
F1	Base	0.5768	0.6998	0.7224	0.7246	0.7043	0.7541	0.7578	0.7264	0.7401	0.7273	0.7328
	Ours	0.6917	0.7140	0.7166	0.7504	0.7477	0.7553	0.7626	0.7541	0.7559	0.7559	0.7637
AP	Base	0.6925	0.7089	0.7264	0.7601	0.7695	0.7943	0.8102	0.8151	0.8000	0.8224	0.8243
	Ours	0.7464	0.7475	0.7637	0.7744	0.7964	0.8084	0.8203	0.8149	0.8206	0.8295	0.8315
Prec	Base	0.7017	0.6195	0.6683	0.6926	0.7425	0.6962	0.6960	0.7583	0.7126	0.7913	0.7992
	Ours	0.7079	0.6626	0.7025	0.6957	0.7556	0.7003	0.7311	0.7838	0.7487	0.7937	0.8098
Recall	Base	0.5103	0.8206	0.7725	0.7589	0.6658	0.8244	0.8289	0.6986	0.7676	0.6715	0.6795
	Ours	0.6761	0.7758	0.7314	0.8299	0.7428	0.8250	0.7549	0.7082	0.7612	0.7234	0.7132

TABLE S2: Multi-label classification evaluation results on the MIMIC-CXR dataset

Metric	Model	Percentage of Training Data										
		0.5%	1%	2%	5%	10%	15%	30%	50%	70%	90%	100%
auROC	Base	0.8593	0.8680	0.8815	0.8906	0.8995	0.9052	0.9083	0.9131	0.9131	0.9149	0.9152
	Ours	0.8723	0.8834	0.8881	0.8980	0.9004	0.9114	0.9148	0.9168	0.9169	0.9188	0.9201
AP	Base	0.4902	0.5174	0.5424	0.5702	0.5811	0.6077	0.6108	0.6215	0.6266	0.6353	0.6379
	Ours	0.5413	0.5582	0.5653	0.5880	0.5858	0.6220	0.6272	0.6376	0.6418	0.6419	0.6427

TABLE S3: Binary classification evaluation results on the Mendeley-V2 dataset

Metric	Model	Percentage of Training Data										
		0.5%	1%	2%	5%	10%	15%	30%	50%	70%	90%	100%
ACC	Base	0.6282	0.6813	0.8436	0.8617	0.8694	0.8715	0.8752	0.8707	0.8614	0.8720	0.8670
	C2L	0.7895	0.8349	0.8755	0.8905	0.8803	0.8926	0.8868	0.8958	0.8910	0.8950	0.9023
	Ours	0.8814	0.8784	0.8958	0.9077	0.9178	0.9104	0.9066	0.9181	0.9157	0.9139	0.9187
auROC	Base	0.5789	0.8698	0.9067	0.9267	0.9274	0.9296	0.9333	0.9311	0.9183	0.9258	0.9321
	C2L	0.7687	0.8275	0.8645	0.8736	0.8681	0.8761	0.8689	0.8800	0.8697	0.8716	0.8873
	Ours	0.9352	0.9409	0.9513	0.9556	0.9611	0.9655	0.9638	0.9668	0.9666	0.9602	0.9613
F1	Base	0.7680	0.7940	0.8763	0.8919	0.8974	0.9000	0.9024	0.8990	0.8943	0.9016	0.8971
	C2L	0.8350	0.8666	0.9013	0.9148	0.9054	0.9165	0.9120	0.9188	0.9164	0.9200	0.9226
	Ours	0.9048	0.9055	0.9193	0.9286	0.9368	0.9316	0.9296	0.9379	0.9355	0.9341	0.9343
AP	Base	0.7113	0.9187	0.9366	0.9503	0.9479	0.9478	0.9510	0.9465	0.9314	0.9391	0.9430
	C2L	0.7914	0.8406	0.8696	0.8745	0.8719	0.8766	0.8702	0.8801	0.8692	0.8699	0.8877
	Ours	0.9553	0.9612	0.9584	0.9641	0.9662	0.9695	0.9690	0.9723	0.9722	0.9613	0.9686
Prec	Base	0.6299	0.6668	0.8666	0.8715	0.8813	0.8765	0.8824	0.8793	0.8551	0.8673	0.8677
	C2L	0.8194	0.8766	0.8943	0.8902	0.8942	0.8920	0.8861	0.8954	0.8808	0.8787	0.9039
	Ours	0.9075	0.8826	0.8934	0.8991	0.9027	0.8929	0.8805	0.8962	0.8999	0.8976	0.8868
Recall	Base	0.9851	0.9818	0.8869	0.9149	0.9151	0.9254	0.9238	0.9221	0.9400	0.9395	0.9338
	C2L	0.8521	0.8573	0.9085	0.9410	0.9171	0.9423	0.9402	0.9436	0.9551	0.9654	0.9427
	Ours	0.9033	0.9310	0.9477	0.9605	0.9738	0.9756	0.9851	0.9844	0.9754	0.9744	0.9779